Praise Worthy Prize

This paper is available online at www.praiseworthyprize.org
International Review of Aerospace Engineering (I.RE.AS.E), Vol. 8, N. 1
ISSN 1973-7459 *February 2015*

The Persistence of Vortex Structures Between Rotating Cylinders in the 10^6 Taylor Number Range

David S. Adebayo, Aldo Rona

Abstract – *The flow in the annular gap $d = R_o - R_i$ between a stationary outer cylinder of radius R_o and a co-axial rotating inner cylinder of radius R_i is characterised at large gap, over the radius ratio (η) range $0.44 \leq \eta \leq 0.53$ and aspect ratio (Γ) range $7.81 \leq \Gamma \leq 11.36$. These configurations are more representative of turbomachinery bearing chambers and large rotating machinery than the journal bearing geometries of narrow gap commonly reported in the literature. Particle Image Velocimetry measurements are taken across the full meridional plane over the Taylor number (Ta) range $258 \times 10^3 \leq Ta \leq 10.93 \times 10^6$, which is 1000 times higher than the critical Taylor number for the onset of the first axisymmetric Taylor instability.*

Well-defined azimuthal vortex structures persist over this high Taylor number range, characterised by a constant number of vortices at a given aspect ratio, vortex core axial and radial motion over time, and mixing between neighbour vortices. This regime, with wavy Taylor vortex flow like features, is defined over the range $1.18 \times 10^6 \leq Ta \leq 6.47 \times 10^6$. These results form a body of experimental evidence from which further progress in the understanding of the wavy Taylor vortex dynamics can be sought, through advanced flow dynamic models that reproduce the persistence of the observed flow features. ***Copyright © 2015 The Authors.***
Published by Praise Worthy Prize S.r.l.. This article is open access published under the CC BY-NC-ND license (http://creativecommons.org/licenses/by-nc-nd/3.0/).

Keywords: *Particle Image Velocimetry, Concentric Cylinders, Wide Gap, Taylor Vortices, Meridional Plane PIV, High Taylor Number Flow*

Nomenclature

d	Gap width between the cylinders
L	Length of the cylinders
N	Number of samples
r	Radial coordinate
Re	Reynolds number
R_i	Inner cylinder radius
R_o	Outer cylinder radius
Ta	Taylor number
Ta_c	First critical Taylor number
T	Torque
W	Work rate input
X	Axial coordinate
Y	Flow-normal coordinate
Z	Transverse coordinate
σ	Standard deviation
$\bar{x}$	Ensemble average of x
x_i	i^{th} data point
Γ	Aspect ratio, L / d
η	Radius ratio, R_o / R_i
θ	Circumferential coordinate, $sin^{-1}(Z / r)$
μ	Dynamic viscosity of the fluid, kg m^{-1} s^{-1}
ν	Kinematic viscosity of the fluid, m^2 s^{-1}
ρ	Density of the fluid, kg m^{-3}
Ω_1	Inner cylinder rotational speed
Ω_2	Outer cylinder rotational speed

I. Introduction

The flow in the gap between concentric independently rotating cylinders features in many aerospace engineering applications. Prime examples are the lubricating flow between rotating shafts of turbo-pumps in rocket engines and of multi-spool turbofan engines and in the bearing housing of high [1] and low [2] bypass aircraft engines.

This flow has attracted great attention over the years. This dates back to 1888 and 1890, when Mallock [3] and Couette [4] conducted independent experiments using concentric rotating cylinders. Taylor's experiment [5] showed that, when the angular velocity of the inner cylinder is increased above a certain threshold, the steady Couette flow becomes unstable.

This leads to a new secondary steady state of axisymmetric flow with regularly spaced vortices (Taylor Vortex Flow). As the Taylor number increases, the axisymmetric time-independent Taylor vortices change to non-axisymmetric unsteady time-dependent wavy Taylor vortices [5]-[8].

The hydrodynamic instability and the transition between the different flow regimes where the outer

Copyright © 2015 The Authors. Published by Praise Worthy Prize S.r.l.
This article is open access published under the CC BY-NC-ND license (http://creativecommons.org/licenses/by-nc-nd/3.0/)
Available online by November 18th, 2015 *doi: 10.15866/irease.v8i1.5288*

cylinder is fixed and only the inner cylinder is rotating $(\mu = \Omega_2 / \Omega_1 = 0)$ can be determined as functions of different non-dimensional parameters.

These parameters are the ratio of the two radii $\eta = R_i / R_o$, the aspect ratio $\Gamma = L(R_o - R_i)$, and the Reynolds number $Re = \Omega_1 R_i d / \nu$ or the Taylor number Ta:

$$Ta = \frac{2\eta^2 d^4}{1-\eta^2}\left(\frac{\Omega_1}{\nu}\right)^2 \quad (1)$$

where R_i and R_o are the radii of the inner and outer cylinder respectively, L is the length of the cylinders, Ω_1 is the rotational speed of the inner cylinder, Ω_2 is the rotational speed of the outer cylinder, d is the gap width, which is the distance between the outer diameter (OD) of the inner cylinder and the inner diameter (ID) of the outer cylinder, and ν is the fluid kinematic viscosity.

Based on these parameters, several regimes of the incompressible flow between two concentric independently rotating cylinders at different radius ratios have been investigated experimentally and documented [5], [8]-[18]. The transition between different flow regimes is reviewed by Di Prima and Swinney [19], Kataoka [20] and Koschmieder [21].

There is a substantial body of literature on configurations with radius ratio over the range $0.60 \leq \eta \leq 0.95$ and aspect ratio $\Gamma \geq 20$, which is likely to be driven by the modelling simplifications that can be used in the cases of small gap ($\eta \to 1$) and large aspect ratio. It is therefore of interest to further explore the flow regime in a flow configuration at a high Taylor number with the radius ratios over the range $0.40 \leq \eta \leq 0.60$ and aspect ratios over the range $7 \leq \Gamma \leq 12$.

As the Taylor number increases, stability theory predicts an increase in the number of natural modes of the flow so that, at a high Taylor number, the flow kinetic energy can distribute among many competing modes.

By analogy with multi-body dynamics from structural mechanics, there may be an expectation that such a large number of modes exchanging energy among one another may result in a disorderly flow, with structures occupying a broad-band wave-number spectrum.

Given that the first instability in the flow between two-coaxial rotating cylinders occurs at a Taylor number of order 10^3, it would perhaps be surprising to find the persistence of structure and order in this flow at a Taylor number above 10^6. Yet the current investigation revealed, perhaps unexpectedly, the presence of well-defined Taylor-like vortices at this high Taylor number range.

The present investigation does not wish to address mode staging over this range of Taylor numbers upfront but aims to provide a detailed body of experimental evidence that constitutes the necessary groundwork for a physics-based interpretation of this flow, upon which the flow dynamic modelling community can test existing models and build improved ones.

This investigation focuses on the meridional plane, which is extensively surveyed by Particle Image Velocimetry (PIV) to characterise the flow features emerging in the low radius ratio and low aspect ratio cylindrical assembly, in which the inner cylinder is rotating and the outer cylinder is fixed.

The main body of this paper is structured into four sections. Section II presents the geometry of the coaxial cylinders used in the experimental work, the test rig instrumentation, and the experimental procedure.

The main experimental results are reported and discussed in section III. Specifically, section III discusses the wavy Taylor vortex flow that develops in the annular region of the coaxial cylinders at $\eta = 0.53$ and $\eta = 0.44$.

Conclusions from this research work are presented in section IV, specifically, on what new knowledge has been exposed.

II. Experimental Facility

Figs. 1 show a schematic of the experimental setup and of the instrumentation. The test rig centrepiece is two rotating concentric cylinders. The air flow between the rotating inner cylinder and the stationary outer cylinder is surveyed by PIV. The flow is illuminated by a laser sheet, imaged by a CCD camera, and analysed by the Dantec Dynamic Studio PIV software version 2.30.

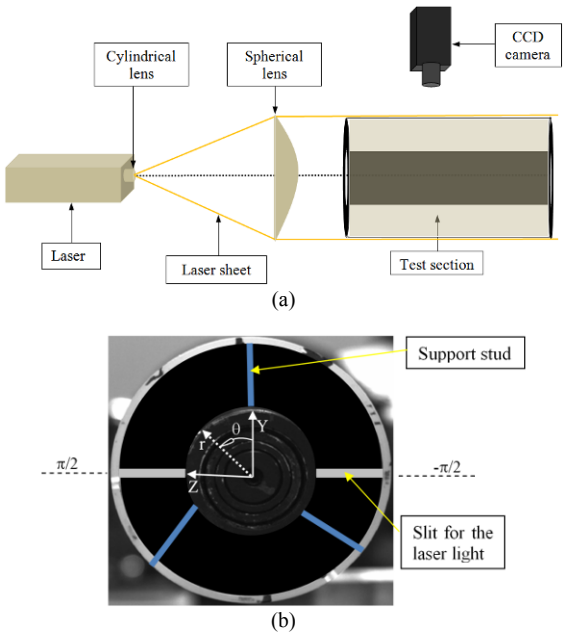

Figs. 1. (a) PIV experimental arrangement for the wide gap Taylor vortex flow apparatus and (b) view from the laser side

II.1. Coaxial Cylinders

A schematic representation of the co-axial cylindrical assembly is shown in Figs. 1 and is defined with respect to the cylindrical reference system (r, θ, Z). The test section consists of a rotating inner cylinder and a stationary outer cylinder.

Copyright © 2015 The Authors. Published by Praise Worthy Prize S.r.l.

The main test rig specifications are summarised in Table I. The thickness of the outer cylinder wall is 3 mm.

The inner cylinder is rotated by a DC electric motor driven by a solid-state speed controller.

The inner cylinder is made of PVC. The inner cylinder is black coated to minimize the reflection from the impinging light sheet from the laser. The outer cylinder is made from a perspex transparent tube to enable visualisation studies and PIV measurements.

TABLE I
GEOMETRY OF THE TEST CASES

Description	Test case 1	Test case 2
Inner cylinder length	0.5 m	0.5 m
Outer cylinder length	0.52 m	0.52 m
Inner cylinder outer diameter	0.05 m	0.05 m
Outer cylinder inner diameter	0.094 m	0.119 m
Gap width	0.022 m	0.032 m

II.2. Instrumentation

The layout of the PIV equipment is shown in Fig. 1(a). The layout is made up of three sections, which are the laser sheet creation section, the test section, and the image recording section. The laser sheet creation section comprises of a two-cavity double-pulsed Nd:YAG Litron L Nano laser and of the laser sheet optics. A trigger rate of 4 Hz is used to generate the light sheet.

A plano-convex spherical lens with an anti-reflective coating is positioned between the laser and the test section as shown in Fig. 1(a) to enable concurrent PIV measurements in the rectangular areas of illuminated flow either side of the inner cylinder. This makes this PIV setup unique with respect to previous experimental investigations of Taylor-Couette flow.

A Dantec Dynamics Studio seeding generator, model 10F03, is used to atomize a mixture of 20% polyethylene glycol (PEG600) and 80% water to produce seeding particles. This resulted in rich and well-diffused seeding, as shown in Fig. 3. The flow is imaged by a Dantec Dynamic Studio FlowSense 4M CCD camera with a resolution of 2048 × 2048 pixels with a 60 mm AF Micro Nikon image lens, operated at a frequency of 4 Hz with an f/4 aperture. The CCD camera is placed at a right angle to the light sheet, as shown in Fig. 1(a). The CCD camera resolution of 2048 × 2048 pixels with a field of view of 250 mm gives a spatial resolution of 0.122 mm/pixel for both test cases.

During image processing, raw particle image pairs are cross-correlated using the adaptive correlation algorithm of Dantec-Dynamics Studio PIV software version 2.30, starting from a 32 × 32 pixel interrogation area and ending with 16 × 16 pixel interrogation areas with a 50% overlap. The average particle displacement was estimated to be approximately six pixels, which is less than 50% of the interrogation area, in agreement with the PIV measurement best practice recommended by Raffel et al. [22]. Validation algorithms are applied to the raw velocity vector map so that erroneous vectors can be detected and removed to produce a validated vector map.

The rotational speed of the inner cylinder shaft was set and monitored by a hand-held laser micro-processor CT6 series tachometer with a measurement range from 3 rpm to 99,999 rpm. During each test, the speed was kept constant within ±1 rpm. The speed was translated to the tangential velocity of the inner cylinder using $v = \Omega_1 R_i$, where v is the velocity (m/s). The room temperature of the air was monitored using a mercury-in-glass thermometer. The temperature of the air and seeding particle mist in the annular gap between the cylinders was measured before and after each set of data acquisition using a K-type thermocouple to check for temperature fluctuations. This was found to be within ±0.5°C of the ambient temperature. The atmospheric pressure of the working fluid was measured using a standard mercury in glass column barometer.

A sanity check was performed on the temperature increase due to the work done on the enclosed fluid by the rotating inner cylinder. An estimate of the torque T normalised by the fluid density ρ, kinematic viscosity ν, and cylinder length L, was obtained from the empirical correlation of Wendt [23]:

$$\frac{T}{\rho \nu^2 L} = 1.45 \frac{\eta^{3/2}}{1-\eta^{7/4}} Re^{1.5} \tag{2}$$

reported in Lathrop et al. [24], for Test case 2.

The highest rotational speed Ω_1 = 650 rpm was used in this estimate, to obtain the highest work rate input to the flow as $W = T\Omega_1 = 1.18 \times 10^{-3}$ Watts. Upon running the experiment for 20 minutes continuously, 1.41 Joules of heat would produce a temperature rise of 0.56 K under adiabatic wall conditions.

This agrees with the small temperature fluctuation measured in experiment. The empirical constant in Wendt [23] has since been derived by analogy to stratified flows in Dubrulle [25], giving further confidence in this estimate.

II.3. Experimental Procedure

PIV measurements for the test cases specified in Table I are conducted along a 250 mm axial length of annulus between the rotating inner cylinder and the stationary outer cylinder. The field of view and the non-dimensional flow parameters for the test cases are summarised in Table II and in Table III respectively. End-walls are fixed to the left and right sides of the stationary outer cylinder. The end-walls are stationary with the outer cylinder. The end-walls are made from black Perspex sheet to prevent laser sheet reflections.

One end-wall has a slit through which the laser sheet enters the annulus, as shown in Fig. 1(b). Measurements are taken as the inner cylinder is rotated at the different angular speeds Ω_1 listed in Table III. Each measurement is taken at constant Ω_1.

Copyright © 2015 The Authors. Published by Praise Worthy Prize S.r.l.

The start-up procedure for all the test cases in this work is a sudden start condition in which the target rotating speed of the inner cylinder is reached within one second. The average room temperature during the experiments was 22.5 ±0.5°C. Since the temperature excursion during the experiments was ±0.5°C, the results have not been corrected for thermal effects.

TABLE II
EXPERIMENTAL FIELD OF VIEW AREA

Description	Test case 1	Test case 2
Axial length of the view area	$0 \le X / R_i \le 10$	$0 \le X / R_i \le 10$
Radial length of the view area	$-1.88 \le r / R_i \le 1.88$	$-2.28 \le r / R_i \le 2.28$
Aspect ratio Γ	11.36	7.81
Radius ratio η	0.53	0.44
Clearance ratio	0.88	1.28

TABLE III
FLOW TEST CONDITIONS

Description	Angular speed (rpm)	Taylor number
Test case 1	500	2.35×10^6
Test case 2	650	10.93×10^6
	500	6.47×10^6
	355	3.26×10^6
	302	2.36×10^6
	214	1.18×10^6
	100	2.58×10^5

The seeding particles in the test section were illuminated by a light sheet of approximately 1 mm thickness shone through the slit as shown in Figs. 1. One hundred image pairs were acquired by the CCD camera controlled by the Dantec Dynamic Studio software.

The image recording method is the double frame-single exposure recording technique. The time interval between the two frames depends on the inner cylinder rotational speed and ranges from 750 μs at 650 rpm to 7500 μs at 100 rpm. The statistical processing of the ensemble of 100 instantaneous velocity fields, data validation, removal of erroneous data, replacement of removed data, and data smoothing was carried out using Dantec Dynamic Studio software. The Dantec Dynamic Studio range validation and the moving average validation algorithms were employed.

The experimental matrix in Table III was constructed to test for the effects of radius ratio and aspect ratio independently from the inner cylinder rotational speed.

Test case 1 and Test case 2 were first run at the same rotational speed. Then these were re-tested at the same Taylor number of 2.35×10^6. The Taylor number effect was further tested by halving the Taylor number from 2.36×10^6 to 1.18×10^6 and from 6.47×10^6 to 3.26×10^6, for test case 2. Finally, test case 2 was run at the upper and lower Ω_1 operational limits of the test rig.

II.4. PIV Measurement Accuracy

The convergence of the PIV data is assessed by testing whether a certain number of PIV raw particle image pairs are enough to obtain a vector map average with a low statistical uncertainty. A converged PIV vector map average is such that, by taking and averaging more PIV vector maps, the average is unchanged.

Previous research by Prasad [26] on PIV vector map averaging indicated that the number of PIV raw particle image pairs required to obtain a converged vector map average ranges from 25 to 250. During initial testing, it was determined that a minimum of 30 images is required to obtain statistically converged engineering accurate PIV results.

In this work, the method used to determine the convergence of the PIV data involves a quantitative analysis of every vector in the vector map, by estimating the mean velocity magnitude and standard deviation from $N > 25$ PIV image snapshots at every single point in the flow. This method involves the following procedure:

1. Acquiring a number of $N > 25$ images and taking the time velocity magnitude ensemble average $\mu(x_i)$ of the N PIV image snapshots at every single point x_i in the flow field.
2. Estimating the standard deviation $\sigma(x_i)$ at every single point x_i.
3. Estimating the relative uncertainty in the mean velocity magnitude $\sigma / \left(\mu\sqrt{N}\right)$ at every single point x_i.
4. Estimating the space averaged value of the relative uncertainty $\sigma / \left(\mu\sqrt{N}\right)$ over all points in the vector map.
5. Steps 1 to 4 are repeated with an increasing number of images N.

Fig. 2 shows the results obtained from implementing this five-step procedure. As shown in Fig. 2, the mean relative uncertainty in the ensemble averaged velocity decreases monotonically with increasing number of PIV images.

In Fig. 2, from the analysis of 30 images, the mean relative uncertainty of the ensemble averaged velocity is about 22%.

As the number of PIV images increases to 90, this value drops to approximately 6.5%.

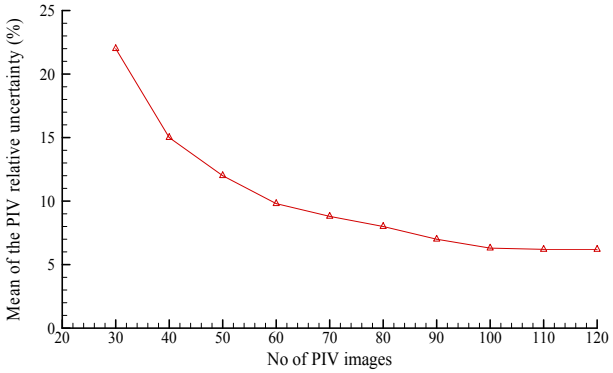

Fig. 2. PIV data convergence based on the mean of the relative uncertainty in the velocity magnitude

Copyright © 2015 The Authors. Published by Praise Worthy Prize S.r.l.

As the number of PIV images increases further, between 100 and 120 images, the mean relative uncertainty in the PIV velocity becomes nearly constant at approximately 5.5%, suggesting that taking more PIV data is unlikely to change this result significantly.

This result shows that the PIV data in this work can be taken as statistically converged when the number of PIV raw particle image pairs is ≥ 100.

III. PIV Results and Discussion

This section discusses the flow features observed in the annulus of the coaxial rotating cylinders, obtained from the PIV measurements. Firstly, the flow regimes that are obtained by running the cylinder of aspect ratio Γ = 7.81 and radius ratio η = 0.44 at different angular velocities are discussed. The range of angular velocities is limited by the solid-state motor controller at the lower end and by the centripetal loads on the rotating cylinder structure at the upper end.

The results reported represent the full operating range available in the experiment. Within this range, the transitions from Taylor vortex flow to wavy vortex flow and, at higher angular speeds, to Turbulent Taylor Vortex Flow, are observed. This is followed by the detailed description of the vortex flow structure for the test cases with aspect ratios Γ = 11.36 and 7.81, and radius ratios η = 0.53 and η = 0.44. All the velocity fields have been normalised by the inner cylinder tangential speed $\Omega_1 R_i$.

The axial length in the PIV results has been normalised by the inner cylinder radius R_i for consistency with the view area normalisation in Table II.

III.1. PIV Flow Regime in the Tests

Many researchers on Taylor vortex instability [21], [27]-[31] attempted to define the thresholds for the onset of Taylor flow regimes in the rotating cylinders based on the Taylor number and radius ratio. Based on the geometry of the apparatus and the flow parameters in Table II and Table III, the Taylor number for the test cases in this work is above the first critical Taylor number Ta_c.

As such, Taylor instability is expected to characterize the flow. This is confirmed by PIV measurements and flow visualisation obtained at different inner cylinder angular velocities Ω_1.

Fig. 3 shows three samples of the imaged flow with PIV seeding at varying angular speeds. The lower portion of the meridional plane, $\theta = -\pi/2$, is reported, with the upper portion giving symmetric results. At Ω_1 = 100 rpm, the result shows typical characteristics of Taylor vortex flow, in which an axial stack of well-defined and ordered Taylor vortex cells develops.

The cells appear as regularly spaced, with well-defined boundaries, resulting in the agglomeration of the PIV seeding towards the cell-centres.

The cell boundaries are neatly displayed by thin regions of rarefied PIV seeding.

These images also suggest that the locations of these boundaries may be stationary, since their motion would have promoted local mixing of the local flow with the neighbouring PIV seeding rich flow. At the higher angular speed of 214 rpm, the flow appears to have changed to a Wavy Taylor vortex flow regime.

The boundary between neighbouring vortex pairs is less clearly defined. The change in seeding particle concentration at the cylinder mid-span region still enables the identification of Taylor vortex cells but time-dependent changes in their axial position and size are likely be promoting axial flow mixing that appears to be more active towards the cylinder end walls. The PIV result at Ω_1 = 214 rpm shows that there is mixing of fluid between the adjacent vortices.

Above this angular speed, the fluid between the adjacent vortices is fully mixed and it is not possible to easily visualise individual vortices, as shown at Ω_1 = 500 rpm in Fig. 3. The PIV seeding becomes rather uniform from 500 rpm, therefore PIV measurements and flow visualisation images obtained at higher rotational speeds are not reported, since, by themselves, they do not provide additional information on the flow.

The instantaneous velocity field was obtained in time at various angular speeds by PIV. The velocity vectors in Fig. 4 shows a sequence of five instantaneous velocity fields. As in Fig. 3, the lower portion of the meridional plane, $\theta = -\pi/2$, is reported, with the upper portion giving symmetric results. These vector maps are representative of the trend observed throughout a set of 100 vector maps at different angular speeds. At each angular speed in Fig. 4, the wall of the rotating inner cylinder is on the top side and the wall of the stationary outer cylinder is on the bottom side.

Fig. 4 shows evidence of transition in the flow regime from Taylor vortex flow to wavy Taylor vortex flow between Ω_1 = 100 rpm and Ω_1 = 214. The velocity vectors of Fig. 4 indicate the wavy Taylor vortex flow regime is maintained over the range Ω_1 = 214 rpm to Ω_1 = 500 rpm. The four pairs of counter-rotating Taylor vortices at Ω_1 = 100 rpm are still observable over this range.

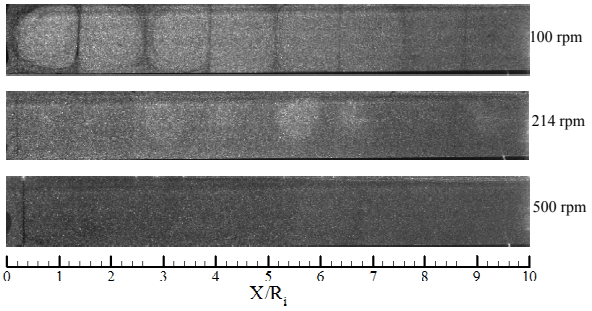

Fig. 3. PIV cross-section of the flow regimes for Taylor vortex flow and Wavy vortex flow

Copyright © 2015 The Authors. Published by Praise Worthy Prize S.r.l.

This pattern is modulated by the waviness of the flow and the boundaries between neighbouring vortices are neither flat nor perpendicular to the cylinder axis. This flow pattern is described in detail in section III.2.

By Ω_1 = 650 rpm, Fig. 4 shows that the flow regime has developed turbulent flow features, as the flow field appears to be characterised by randomness and distorted regular Taylor vortices can be clearly seen. There is breakdown of axial periodicity in the flow pattern.

The flow field at Ω_1 = 650 rpm shows large-scale motion with many small-scale vortices embedded within it. This is a recognisable feature of turbulent flow in which the time evolution is stochastic rather than deterministic. The flow field is changing so that it was not possible to observe the recurrence of any one pattern of vortices, or vector field image, in all the 100 PIV snapshots. In some snapshots, Taylor vortices are not identifiable in the fully irregular turbulent flow and, at other times, distorted Taylor vortices are present that cannot be easily distinguished in the background turbulent flow. This flow pattern can no longer be described by well-defined Taylor vortices, although structures associated with the Taylor vortices remain. This is indicative of a further change in the flow regime to Turbulent Taylor vortex flow.

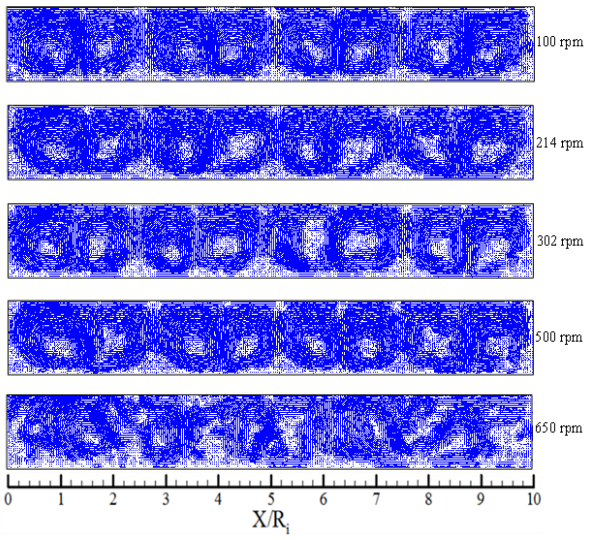

Fig. 4. Instantaneous velocity vectors in the meridional plane ($\theta = -\pi / 2$) when the inner cylinder rotates at Ω_1 = 100 rpm, 214 rpm, 302 rpm, 500 rpm, and 650 rpm. Γ = 7.81, η = 0.44

By altering the rotational speed Ω_1, this experiment has enabled to observe the transition from Taylor vortex flow to Wavy Taylor vortex flow and, subsequently to Turbulent Taylor vortex flow. This has determined the approximate range of Ω_1 for Wavy Taylor vortex flow.

The remainder of this paper is concerned with examining closely the vortex flow structures for two different test cases Γ = 11.36, η = 0.53 and Γ = 7.81, η = 0.44 at Ω_1 = 500 rpm, with specific attention to the fluid dynamics observable from PIV.

III.2. Characteristics of the Flow Regime in the Tests

On the basis of the Taylor number and the radius ratio, the current test cases Γ = 11.36 and Γ = 7.81 could fall respectively into the Modulated Wavy Vortex Flow (MWVF) and Turbulent Taylor Vortex Flow (TTVF) flow regimes according to the flow stability map reported in Andereck et al. [13]. However, the analysis presented in sections III.3 and III.4 shows evidence of Wavy Vortex Flow for both test cases.

III.3. Analysis of the Flow Structures at 500 rpm

The evolution of the instantaneous flow field in time was obtained in order to improve the understanding of the flow regime that develops in the annular region of these test cases. The velocity vectors in Figs. 5 show a sequence of three normalised instantaneous velocity fields in the meridional plane $\theta = -\pi / 2$.

The meridional plane is the plane imaged by the CCD camera in the experimental setup of Figs. 1. The velocity fields are taken in quick succession at recording times t = 0.0 s, t = 0.25 s, and t = 0.50 s, with the time increasing in Fig. 5 from bottom to the top, as shown by the arrows. In each time frame in Figs. 5, the wall of the rotating inner cylinder is on the top side and the wall of the stationary outer cylinder is on the bottom side. Fig. 5(a) and Fig. 5(b) show respectively six pairs and four pairs of counter-rotating Taylor vortices in the annulus between the rotating inner cylinder and the stationary outer cylinder for test cases Γ = 11.36 and Γ = 7.81.

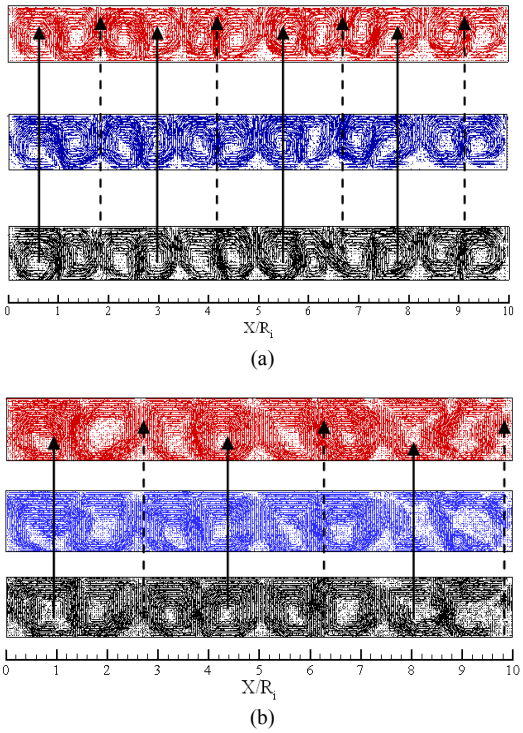

Figs. 5. Instantaneous velocity vectors in the meridional plane ($\theta = -\pi / 2$). (a) Γ = 11.36, η = 0.53 and (b) Γ = 7.81, η = 0.44. Time sequence t = 0.00 s (bottom), t = 0.25 s (middle) and t = 0.50 s (top)

Copyright © 2015 The Authors. Published by Praise Worthy Prize S.r.l.

The flow in the middle of each vortex pair is driven from the inner cylinder towards the outer cylinder by the vortex pair induced velocity. This creates outward flow (outflow) regions. Similarly, neighbouring vortex pairs drive the flow from the outer cylinder towards the inner cylinder, creating inward flow (inflow) regions.

The flow pattern in Figs. 5 is characterized by vortex contraction, expansion, and undulation. There is significant cyclic transport of fluid between vortices. The boundaries between adjacent vortices are dynamic, with their position and orientations changing with time.

The inflow and outflow regions are not uniform and not perpendicular to the cylinder walls. As such, the inflow and outflow boundaries are twisted at an angle.

At the boundaries of the inflow and outflow regions, there is a slight displacement of the radially aligned velocity vectors in the axial direction with time, though not as evident as the vortex centre motion, as indicated by the dashed line arrows in Figs. 5.

The observed flow features are evidence of the presence of azimuthal waves that characterize the wavy vortex flow regime described in section I. In Figs. 5, the magnitude of the oscillations of the inflow and outflow boundaries and of the vortex centres are not so significant as to fully disrupt the main vortex flow pattern, which prevents the flow from becoming fully random and stochastic.

Considering the Taylor number at which the measurements are taken, the vortex centre motion suggests that the flow regime is the wavy vortex flow that probably re-emerges at high Taylor numbers.

This may be related to the re-emergence of azimuthal waves at high Reynolds numbers and larger aspect ratios reported by Walden and Donnelly [12], Takeda [32], Lewis and Swinney [33], and Wang et al. [34]. Alternatively, the sudden start condition of this experiment may have by-passed some of the intermediate stages of the Taylor vortex flow development during the fast spooling-up, with the flow settling as a wavy vortex flow.

The type of fluid mixing between adjacent vortices reported by Wereley and Lueptow [35] at a high Taylor number is evident in the instantaneous velocity vectors in Figs. 5. The same authors observed that the axial motion of the vortex centres is always greater than the radial motion of the vortex centres at all Taylor numbers of their experiment.

This is not the case in this work.

However, the flow pattern throughout the annulus exhibits the main characteristics of wavy vortex flow.

The flow patterns in Figs. 5 show that it is possible to observe wavy vortex flow for concentric cylinders with low aspect ratio $\Gamma < 25$, where Walden and Donnelly [12] did not observe wavy vortex flow in their experiments in which $\eta = 0.875$.

The discrepancies in flow regime between this work and that by Wereley and Lueptow [35] and by Walden and Donnelly [12] may be attributed to the differences in the radius ratio and aspect ratio among these studies.

III.4. Time Averaged Velocity Vector Maps

Figs. 6 display the normalised ensemble averaged velocity vector maps obtained from 100 pairs of PIV images in the meridional plane of the annulus for the present test cases.

In Figs. 6, the radial motion induced by the Taylor vortices convects the fluid with high azimuthal momentum near the rotating inner cylinder radially outward, in the outflow regions between two adjacent vortices in each vortex pair. Similarly, low speed fluid near the stationary outer cylinder is convected radially inward in the inflow regions between two adjacent pairs of vortices. This redistributes the angular momentum of the fluid across the annulus.

The consequent redistribution of flow mass across the annulus affects the inward flow and the outward flow velocity distribution. Thus, the radial outflow between the vortices is stronger than the radial inflow, as evidenced by the length of the velocity vectors in Figs. 6 close to the outer cylinder wall. The strong radial motion at the outflow boundaries and the mixing of fluid between the adjacent vortices are responsible for the azimuthal waviness observed in Figs. 6 [35]-[38], which is displaced on the measurement plane by the axial change in the vortex centres between $\theta = -\pi/2$ and $\theta = \pi/2$.

The vortices in Figs. 6 are organised in a definite pattern, in which the centres of a pair of vortices are radially displaced in an alternate manner, such that when the centre of one vortex is displaced toward the outer cylinder, the centre of the next vortex inbounds is displaced toward the wall of the inner cylinder.

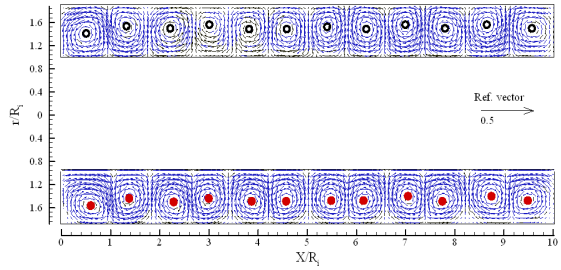

(a) $\theta = -\pi/2$ (o), $\theta = \pi/2$ (•)

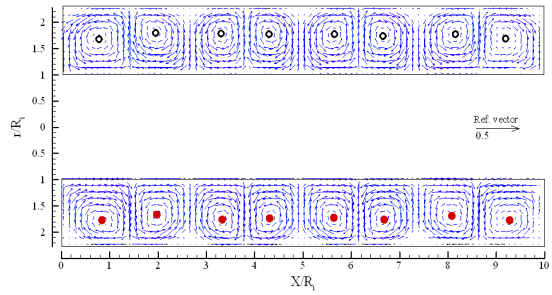

(b) $\theta = -\pi/2$ (o), $\theta = \pi/2$ (•)

Figs. 6. Normalised time average of the velocity vectors from the PIV measurement in the meridional plane of the annulus, (a) $\Gamma = 11.36$, $\eta = 0.53$ and (b) $\Gamma = 7.81$, $\eta = 0.44$.

The reference velocity vector is $0.5\,\Omega_1 R_i$

Copyright © 2015 The Authors. Published by Praise Worthy Prize S.r.l.

The instance at which the vortex centre is closest to a wall corresponds to the instance that the fluid is winding around the opposite side of the vortex. This results in an axial transport of the flow in-bounds at $\theta = -\pi/2$ and out-bounds at $\theta = \pi/2$. These two mass fluxes ought to balance each other to satisfy the continuity of mass in this enclosed flow. The radial translation of the vortex centres may be related to the degree of axial flow [35].

In the regions near the end walls in Fig. 6(a), the radial motion of the vortex centres can be described as being out of phase because where one vortex moves radially outward, the adjacent vortex moves radially inward.

The transfer and mixing of fluid between adjacent vortices takes place in both the outflow and inflow regions, indicating that vortex cells are not independent in these two regions.

The velocity vector map of Fig. 6(b), for the test case $\Gamma = 7.81$, is organised in a similar pattern as the velocity vector map in Fig. 6(a). The salient flow features in these regions are the same as the ones discussed in the context of Fig. 6(a). The significant radial variation of the vortex centre position along the axis approaching the end-walls in Fig. 6(b) indicates that the flow regime is still that of a wavy vortex flow. Close examination of the velocity field in Fig. 6(b), Fig. 5(b) and the analysis of the location of the vortex centres in Figs. 7 show the radial displacement of the vortices. The axial displacement of the vortex centres at $\theta = \pm\pi/2$ is not as evident in Fig. 6(b) as in Fig. 5(b). However, from Fig. 5(b) and Figs. 7, there is clear evidence of axial and radial displacement as well as waviness in the flow at $\Gamma = 7.81$.

The results obtained at $\Gamma = 7.81$ suggest that the flow between neighbouring vortex pairs is coupled to a less degree close to the outer cylinder than close to the inner cylinder. Such radial dependence of the degree of interaction between neighbouring Taylor vortex pairs may have a practical implication for the development of successful models of the Taylor cell dynamics in wide gap configurations.

III.5. Vortex Centres

A distinct pattern in Figs. 5 and Figs. 6 is the spatial oscillation of the Taylor vortices resulting in the radial and axial displacement of the vortex centres. For instance, in Figs. 6, the radial displacement of the vortices is clearly shown by the location of the vortex centres. Comparing the vortices at $\theta = -\pi/2$ and those at $\theta = \pi/2$ with one another at the same axial position in Figs. 6, an axial oscillation of the vortex centre position is not so evident in these time-averaged velocity vector maps, whereas it is more evident in the time-dependent velocity vector maps of Figs. 5. The flow patterns in Figs. 5 show that the vortex centres oscillate in the radial and axial directions over time, as shown by the solid arrows.

This is evidenced by the shift in the radial and axial position of the vortex centres in the time sequence of Figs. 5 about the solid arrows.

The shifting of the vortex centres in the axial direction is more prominent in the test case $\Gamma = 7.81$ than that in the test case $\Gamma = 11.36$.

In order to improve the understanding of the degree of the spatial oscillation in the test cases, the locations of the Taylor vortex centres for the coaxial cylinders test cases $\Gamma = 11.36$ and $\Gamma = 7.81$ are estimated. In this study, the radial and axial coordinates of the Taylor vortex centres are determined by the cross-sectional lines algorithm described by Vollmers [39], which is based on obtaining the difference between vortex induced velocity extrema.

The axial coordinate X_c and the radial coordinate r_c of each of the vortex centre are used to mark the centres of the vortices in Figs. 6.

The same algorithm was also applied to 100 instantaneous velocity vector maps of the like of Figs. 5. The procedure followed to determine the location of vortex centres is detailed in Adebayo [40].

Fig. 7(a) and Fig. 7(b) display the spread of the vortex centre positions in the axial and radial directions in the meridional plane at the lower ($\theta = -\pi/2$) channel from Figs. 5 and from likewise instantaneous PIV vector maps. The spread is estimated from the analysis of 100 maps. The vertical orange bars show the minimum and maximum radial displacement of each vortex centre at $\theta = -\pi/2$ estimated from one standard deviation of the 100 vector maps, while the horizontal blue bars represent the minimum and maximum axial displacement of each vortex centre mean value at $\theta = -\pi/2$.

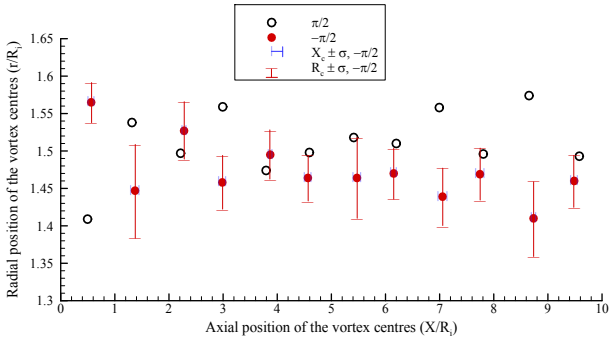

(a)

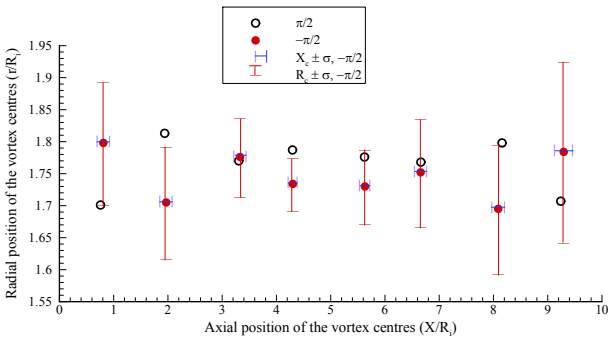

(b)

Figs. 7. Spread of vortex centre axial and radial positions in the meridional plane at $\theta = -\pi/2$ for the test cases (a) $\Gamma = 11.36$ and (b) $\Gamma = 7.81$

Copyright © 2015 The Authors. Published by Praise Worthy Prize S.r.l.

The bars in Figs. 7 show the extent by which the vortex centres are displaced radially and axially in the annulus.

The displacement of the vortex centres in these directions results in the spread rate about the vortex centre mean value in the axial and radial directions shown by the plots in Figs. 7.

In agreement with the observation made in Figs. 6, the time average positions of the vortex centres are displaced toward the inner cylinder and toward the outer cylinder in an alternating fashion, so that where the mean position at $\theta = \pi / 2$ is towards the inner rotating cylinder at a given X / R_i, the corresponding mean radial position of the vortex centre at $\theta = -\pi / 2$ at the same X / R_i is towards the stationary outer cylinder.

In Fig. 7(a) and Fig. 7(b), although the spread of vortex centres in the axial and radial positions of the meridional plane at the upper ($\theta = \pi / 2$) channel was not estimated, these figures clearly indicate that there would be an overlap in the spread for both the upper and lower channels.

The axial displacement of the vortex centres cannot be compared directly with the radial displacement of the vortex centres in Figs. 7, as both axes are not on the same scale.

The axial variation of the vortex centre appears to be small compared to the axial spacing of the vortices.

IV. Conclusion

The majority of the past investigations on the Taylor vortex flow focussed on large aspect ratio and low radius ratio configurations, representative of the annular flow in oil wells, or on high radius ratio (small gap width) configurations, relevant to journal bearing flows.

This paper addressed the comparatively under-explored low aspect ratio and low radius ratio (wide gap width) configuration, relevant to important engineering applications such as lubrication bearing chambers. Particle Image Velocimetry was applied to the flow between concentric cylinders in two test cases of radius ratio η = 0.53 and 0.44, aspect ratio Γ = 11.36 and 7.81, speed ratio μ = 0, and Taylor number range $258 \times 10^3 \leq Ta \leq 10.93 \times 10^6$.

These PIV measurements show the transition from a pattern of steady Taylor vortices to a wavy Taylor vortex like regime and, subsequently, to turbulent Taylor vortex flow, as the rotational speed of the inner cylinder was increased in steps through the operating range of the test rig. For both test cases, at Ω_1 = 500 rpm, a flow with wavy Taylor vortex flow like features is observed at a Taylor number higher than the one indicated by Andereck et al. [13] and by Di Prima and Swinney [19] for transition to Modulated Wavy Vortex Flow.

At the low radius ratio of these tests, wavy vortex flow was observed at an aspect ratio less than 25, where Walden and Donnelly [12] did not observe wavy vortex flow in their experiments in which η = 0.875.

Whilst it is known that, in general, the radius ratio and the aspect ratio can influence the flow regime in the annular gap between concentric cylinders, this experiment gives the first substantial experimental evidence of this occurrence in these high radius ratio and low aspect ratio configurations. The characterising flow features of wavy Taylor vortex flow were also observed when the Taylor number was varied independently from the radius ratio and the aspect ratio.

This work has provided a body of experimental evidence that poses questions of both theoretical and practical nature. From the theoretical viewpoint, it challenges the flow dynamic modellers on whether these features are rendered by the current models. The presence of two confluent streams in the inflow region may indicate a degree of coupling between neighbouring vortex cells that is radially varying and perhaps lower towards the outer cylinder wall. This may prompt further progress in modelling wavy Taylor vortex flow, leading to a more complete understanding of the flow dynamics.

The experimental evidence is of practical relevance to the design of oil bearing chambers. Specifically, the flow mixing between neighbouring vortex cells and possibly the heat transfer rate are likely to be lower than from a pattern of regularly spaced vortices in the axial direction.

This influences the migration of metal contaminants between cells. A single magnetic plug is often used to remove these particles, under the assumption that substantial flow mixing between cells takes place. This poses the question of how the newly observed flow features affect the effectiveness of this single point metal particle collection.

Acknowledgements

This project has been supported by a Specific Targeted Research Project of the European Community's Sixth Framework Programme under project number 32669 (PROVAEN). The experimental rig was fabricated and instrumented with help from Mr. Paul Williams, Thermofluids experimental officer, Mr. Dipak Raval and Mr. Julian Jones, engineering technicians, and the mechanical engineering workshop. EPSRC SRIF2 laser equipment components were used. The laser traverse was on loan from the Greenbank Group Ltd.

References

[1] Hassan, H.Z., Gobran, M.H., Abd El-Azim, A., Simulation of a transonic axial flow fan of a high bypass ratio turbofan engine during flight conditions, (2014) *International Review of Aerospace Engineering,* 7 (1), pp. 17-24.

[2] M. A. Aziz, Farouk M. Owis, M. M. Abdelrahman, Preliminary Design of a Transonic Fan for Low By-Pass Turbofan Engine, (2013) *International Review of Aerospace Engineering (IREASE),* 6 (2), pp. 114-127.

[3] A. Mallock, Determination of the viscosity of water, *Proceedings of the Royal Society of London 45 (1888), 126-132*.

[4] M. Couette, Études sur le frottement des liquides, *Ann. Chim. Phys. 6 (1890), 433-510*.

Copyright © 2015 The Authors. Published by Praise Worthy Prize S.r.l.

[5] G. I. Taylor, Stability of a viscous liquid contained between two rotating cylinders, *Philos. Trans. R. Soc. London A223 (1923), 289-343*.
[6] A. H. Nissan et al, The onset of different modes of instability for flow between rotating cylinders, *Al. Ch. E. J. 9 (1963), 620-624*.
[7] K. W. Schwarz et al, Modes of instability in spiral flow between rotating cylinders, *Journal of Fluid Mechanics 20 (1964), 281-289*.
[8] D. Coles, Transition in circular Couette flow, *Journal of Fluid Mechanics 21 (1965), 385-425*.
[9] H. A. Snyder, Waveforms in rotating Couette flow, *International Journal of Non-linear Mechanics 21 (1970), 659-685*.
[10] P. J. Gollub and H. L. Swinney, Onset of turbulence in rotating fluid, *Physical Review Letters 35 (1975), 927-930*.
[11] P. R. Fenstermacher et al, Dynamical instabilities and the transition to chaotic Taylor vortex flow, *Journal of Fluid Mechanics 94 (1979), 103-129*.
[12] R. W. Walden and R. J. Donnelly, Reemergent order of chaotic circular Couette flow, *Physical Review Letters 42 (1979), 301-304*.
[13] C. D. Andereck et al, Flow regimes in a circular Couette system with independently rotating cylinders, *Journal of Fluid Mechanics 164 (1986), 155-183*.
[14] R. Tagg, The Couette-Taylor problem, *Nonlinear Science Today 4 (1994), 1-25*.
[15] J. M. Nouri and J. H. Whitelaw, Flow of Newtonian and non-Newtonian fluids in a concentric annulus with rotation of the inner cylinder, *Journal of Fluids Engineering 116 (1994), 821-827*.
[16] A. Racina et al, Experimental investigation of flow and mixing in Taylor-Couette reactor using PIV and LIF methods, *International Journal of Dynamics Fluids 1 (2005), 37-55*.
[17] S. S. Deshmukh et al, Computational flow modeling and visualization in the annular region of annular centrifugal extractor, *Industrial and Engineering Chemical Research 46 (2007), 8343-8354*.
[18] S. S. Deshmukh et al, Flow visualization and three-dimensional CFD simulation of the annular region of an annular centrifugal extractor, *Industrial and Engineering Chemical Research 47 (2008), 3677-3686*.
[19] H. L. Swinney and J. P Gollub, *Hydrodynamic instabilities and the transition to turbulence*, second ed. (Springer-Verlag, New York, 1981, pp. 139-180).
[20] N. P. Cheremisinoff, *Encyclopedia of Fluid Mechanics*, (Gulf Publishing Company, Houston, 1985, pp. 237–273).
[21] E. L. Koschmieder, Benard cells and Taylor vortices, first ed. (Cambridge University Press, Cambridge, 1993).
[22] M. Raffel, *Particle Image Velocimetry - A practical guide*, second ed. (Springer, Berlin, 2007).
[23] F. Wendt, Ingenieur-Archiv *4 (1933), 577*.
[24] D. P. Lathrop et al, Transition to shear-driven turbulence in Couette-Taylor flow, *Physical Review A 46 (1992), 6390-6405*.
[25] B. Dubulle, Momentum transport and torque scaling in Taylor-Couette flow from analogy with turbulent convection, *European Physical Journal B 21 (2001), 295*.
[26] A. K. Prasad, Particle image velocimetry, *Curr. Sci. 79 (2000), 51-60*.
[27] P. H. Roberts, The solution of the characteristic value problem, *Proceedings of the Royal Society of London A283 (1965), 550-556*.
[28] J. E. Burkhalter and E. L. Koschmieder, Steady supercritical Taylor vortex flow, *Journal of Fluid Mechanics 58 (1973), 547-560*.
[29] G. P. Smith and A. A. Townsend, Turbulent Couette flow between concentric cylinders at large Taylor numbers, *Journal of Fluid Mechanics 123 (1982), 187-217*.
[30] A. Recktenwald et al, Taylor vortex formation in axial through-flow: Linear and weakly nonlinear analysis, *Physical Review E 48 (1993), 4444 - 4454*.
[31] B. Haut et al, Hydrodynamics and mass transfer in a Couette-Taylor bioreactor for the culture of animal cells, *Chemical Engineering Science 58 (2003), 774 -784*.
[32] Y. Takeda, Quasi-periodic state and transition to turbulence in a rotating Couette system, *Journal of Fluid Mechanics 389 (1999), 81-99*.
[33] G. S. Lewis and H. L. Swinney, Velocity structure functions, scaling, and transitions in high-Reynolds number Couette-Taylor flow, *Physical Review E 59 (1999), 5457-5467*.
[34] L. Wang et al, Reappearance of azimuthal waves in turbulent Taylor-Couette flow at large aspect ratio, *Chemical Engineering Science 60 (2005), 5555-5568*.
[35] S. T. Wereley and R. M. Lueptow, Spatio-temporal character of non-wavy and wavy Taylor-Couette flow, *Journal of Fluid Mechanics 364 (1998), 59-80*.
[36] P. S. Marcus, Simulation of Taylor-Couette flow. Part 2. Numerical results for wavy vortex flow with one travelling wave, *Journal of Fluid Mechanics 146 (1984), 65-113*.
[37] C. A. Jones, The transition to wavy Taylor vortices, *Journal of Fluid Mechanics 157 (1985), 135-162*.
[38] K. T. Coughlin and P. S. Marcus, Modulated waves in Taylor-Couette flow Part 2. Numerical simulation, *Journal of Fluid Mechanics 234 (1992), 19-46*.
[39] H. Vollmers, Detection of vortices and quantitative evaluation of their main parameters from experimental velocity data, *Measurement Science and Technology 12 (2001), 1199-1207*.
[40] D. S. Adebayo, *Annular flows and their interaction with a cylindrical probe*, Ph.D. dissertation, Dept. Eng., University of Leicester, Leicester, UK, 2012.

Authors' information

Department of Engineering, University of Leicester, LE1 7RH, UK.

Aldo Rona received a Bachelor of Engineering in aeronautics from City University, London, UK, in 1993 and a Ph.D. in computational fluid dynamics of unsteady compressible flows from Southampton University, Southampton, UK, in 1997. As EPSRC Research Fellow at the Department of Aeronautics and Astronautics, University of Southampton, (1996-1997), he studied vortex boundary layer interactions by laser velocimetry. He developed time-resolved numerical models of unsteady transonic flows for high speed air transport applications as EU Marie Curie Fellow at the Department of Aeronautics and Aerospace, von Karman Institute for Fluid Dynamics, Belgium, in 1998. He joined the Department of Engineering at the University of Leicester, Leicester, UK, in 1998 as Lecturer where he has been working as Senior Lecturer since 2010. He has actively pursued research in unsteady flows relevant to air transport operations, with a focus on jets and jet noise, cavity flow and its contribution to airframe noise, and over-shroud leakage flow in axial turbines. Dr. Rona is a chartered engineer (CEng) and member of the Royal Aeronautical Society.

David S. Adebayo received a Bachelor of Engineering (BEng) degree from the University of Ilorin, Nigeria in 1992, a Master of Science in advanced mechanical engineering from the University of Leicester, Leicester, UK, in 2005 and a Ph.D. in engineering from the University of Leicester, Leicester, UK, in 2012.
Prior to his Master and Ph.D. degrees at the University of Leicester, he worked in many engineering industries in collaboration with international organisations for more than a decade and served in various capacities managing several projects. He has been Honorary Visiting Fellow of the University of Leicester since 2013 and teaching MEng aerospace engineering students. He has actively pursued research in annular flows and their interaction with a cylindrical probe, with application to aerospace engineering.
Dr. Adebayo is affiliated to the IMechE and a member of professional bodies: Nigeria Society of Engineers (NSE) and Council for the Regulation of Engineering (COREN).

Copyright © 2015 The Authors. Published by Praise Worthy Prize S.r.l.